Efficient multiresonant laser isotope separation

Aaron D. Barr,[1,*] Simon Rochester,[2] Dmitry Budker,[3,4,5,6] and Mark G. Raizen[1,†]

[1] *Dept. of Physics, University of Texas at Austin, Austin, Texas 78712, USA*

[2] *Rochester Scientific, LLC*

[3] *Johannes Gutenberg-Universität Mainz, 55122 Mainz, Germany*

[4] *Helmholtz Institute Mainz, 55099 Mainz, Germany*

[5] *GSI Helmholtzzentrum für Schwerionenforschung GmbH, 64291 Darmstadt, Germany*

[6] *Department of Physics, University of California, Berkeley, California 94720-7300, USA*

(Received 12 June 2025; revised 12 August 2025; accepted 29 August 2025; published 30 September 2025)

A method for efficient isotope separation is proposed, based on efficient photoionization of atoms by a continuous-wave laser using resonant enhancement in an ultralarge volume optical cavity. This method should enable higher efficiency than the existing state of the art and could be used as an alternative to radiochemistry. It should also allow separation of radioisotopes that are not amenable to standard radiochemistry, with important implications for medicine.

DOI: 10.1103/djk8-pv16

I. INTRODUCTION

Most elements in the periodic table have several stable isotopes differing from each other by the number of neutrons in the nucleus. There are 254 stable isotopes that are found with varying natural abundances, created in the early universe. Beyond stable isotopes, the list is greatly expanded when one includes radioisotopes of the elements, with half-lives ranging from short (less than a second) to intermediate (days or weeks) and long (years). These radioisotopes typically decay by emission of high-energy particles, including electrons (betas), helium nuclei (alphas), and photons (gammas) [1].

Isotopes are a great resource for humanity. In medicine, therapy with radioactive seeds is used for treating tumors [2]. Radioimmunotherapy, where cancer cells are directly targeted and destroyed, offers treatment for metastatic cancer, and holds potential for even higher efficacy as targeting molecules are improved [3]. Medical imaging with radioisotopes provides diagnosis of illness [4]. Stable isotopes can be used as tracers for the diagnosis and treatment of metabolic disorders, and for early detection of disease by a change in isotopic ratios in the body [5].

The first step towards realizing any applications of isotopes is the ability to separate them, a difficult task due to their nearly identical physical and chemical properties. The two main methods to date are the calutron, invented over 80 years ago by Ernest Lawrence [6], and the gas centrifuge, which is only applicable to a few elements in the periodic table that have gas-phase compounds at room temperature [7]. The calutron is the most general method for isotope separation, now referred to as electromagnetic isotope separation (EMIS). While EMIS is an established method, it is energy intensive due to the large magnetic field required over the entire ionization volume. The large-scale machines in the USA and elsewhere were shut down in the late 1990s due to their high operating costs, leaving only Russia as the global source. Near-total dependence on subsidized Russian machines created a fragile supply chain [8]. In recent years, the US Department of Energy has invested significant resources towards construction of new EMIS units to address growing demand, and this effort has been successful [9].

Motivated by the desire to make isotope separation machines more compact and energy-efficient, the possibility of using lasers for this purpose has been the topic of intense effort. Previous work on laser separation of isotopes relied on multiphoton ionization with pulsed lasers [10]. In some variations, continuous-wave (CW) lasers were proposed and used to achieve isotopically selective optical pumping into metastable states, but the final step of laser ionization was always accomplished with a pulsed nanosecond laser [11–14]. This method, known as atomic vapor laser isotope separation (AVLIS), was developed for uranium separation by large-scale government programs as an alternative to the gas centrifuge. Ultimately, these large-scale AVLIS programs failed and were abandoned. Proposals and demonstrations of AVLIS with various stable isotopes continue to this day, but AVLIS has never transitioned from numerical simulations and demonstration experiments to commercial production despite many years

*Contact author: aaronbarr8@utexas.edu

†Contact author: raizen@physics.utexas.edu

of effort. This may be due to the requirement for high laser power needed for efficient ionization, combined with low repetition rate of the pulsed lasers. The need for continuous operation demands robust lasers and other components. Meanwhile, there has been great progress in solid-state laser technology over the past years, providing robust platforms of tunable CW lasers at several-watt power levels. These include semiconductor diode lasers [15] and vertical external cavity surface emitting (VECSEL) lasers [16].

In recent years, an alternate method of laser isotope separation was developed by our group, magnetically activated and guided isotope separation (MAGIS) [17,18]. This uses lasers to change how atoms respond to a magnetic field through a process known as magnetic-state optical pumping. Desired isotopes are then separated using arrays of permanent magnets, which act as a guiding track. The isotopically selective laser excitation relies on an isotope shift of atomic resonant frequencies that depends on the mass number of the nucleus. The isotope shifts are typically in the range of 1 GHz out of an optical frequency, so only one part in 10^5, but that shift is larger than the Doppler profile of an atomic beam. MAGIS relies on permanent rare-earth magnets to create a large field close to the surface of the magnets. It therefore does not consume much energy, unlike the calutron, except for vaporization of the element in a crucible, operation of the vacuum pumps, and the lasers (taken together, these are typically around three orders of magnitude smaller than electrical consumption by the calutron). MAGIS was proven in the laboratory [19] and protected by an issued patent [20]. MAGIS is used to produce commercial quantities of Yb-176 at high enrichment needed for production of the radioisotope Lu-177 which is used for cancer therapy [21].

The limitations of MAGIS are primarily due to the currently available strength of permanent rare-earth magnets. First, to reach the field strengths required for separation, the atoms must be collimated in one dimension to less than 20 mrad so that they may be aimed at small grazing angles of incidence to the magnetic array. This collimation also reduces atomic flux. Laser cooling can brighten the beam considerably, but at the cost of much higher laser power [22,23]. Second, scaling up production requires large magnetic arrays, precluding the application of MAGIS for separation of radioisotopes. The safe handling of radioisotopes, especially gamma emitters, requires a special enclosure that provides radiation shielding for operators together with robotic control, known as a hot cell [24].

In this paper, we propose a method for isotope separation based on photoionization of atoms that should resolve the current limitations of AVLIS. The method, multiresonant laser isotope separation (MRLIS), is described in detail for a generic case, and then specifically for strontium (Sr) isotope separation. Applications to several isotopes are outlined, both stable and radioisotopes, as an alternative to radiochemistry.

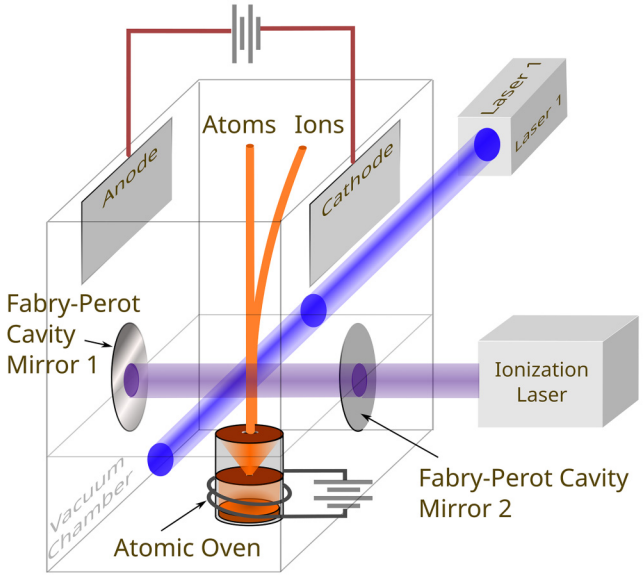

FIG. 1. Schematic of proposed experimental setup. An atomic oven inside a vacuum chamber produces an effusive atomic beam that is collimated. The blue laser excites the desired atoms. The ionizing laser (purple) is enhanced in a large mode-volume cavity. Ionized atoms are collected on a cathode.

II. MRLIS DESCRIPTION

The goal is efficient ionization of the desired isotopes with lasers, and their separation from the atomic beam with an electric field so they can be collected. The approach used in the past for laser ionization relied on a fast sequence of high-intensity nanosecond pulsed lasers. The excitation of atoms from the ground state using resonant atomic transitions can be efficient, but the problem was with the last step of photoionization.

We propose to use CW lasers to drive atomic transitions, combined with long interaction time in ultralarge-volume resonant cavities. This paradigm has many advantages, including the use of reliable solid-state lasers and predicted high ionization efficiency.

A schematic of the proposed setup is shown in Fig. 1. The first step in the process is excitation of the desired isotopes from their ground electronic state to an excited electronic state. This is not fundamentally different from what is done in AVLIS, especially with recent proposals to use CW lasers or time-delayed pulsed lasers to pump into a metastable atomic state [11,12]. In some cases, a two-step excitation from the ground state should be employed, which can be driven efficiently using stimulated Raman adiabatic passage [25].

The last step is photoionization, which is nonresonant and typically requires a high-power pulsed laser. We propose to use an optical resonator to boost the laser power by a factor of at least 200. The problem with optical resonators, also known as Fabry-Perot interferometers, is that the Gaussian waist scales as the product of cavity length and mirror radius of curvature to the one-fourth power [26]. The resulting beam waist is usually in the region of 100 μm, which would intersect only a small fraction of the atomic beam and result in low average ionization probability. One option is to use a cavity with two flat mirrors and an intracavity lens, but the beam waist is of the order of several millimeters [27]. The alternative is to make the radius of curvature very large using thin-film deposition. In previous work, a radius of curvature of 10 km was demonstrated [28], but could be made much larger by using flat mirrors. Such a configuration is usually called an etalon, but in the past, it has been used with low reflective coatings or none at all. Such a configuration with high-reflectivity mirrors was first considered in Ref. [29], though applications to laser ionization were not proposed.

The only condition for resonance is that there be a uniform phase front to the beam, and the overall length of the cavity be an integer multiple of half-wavelengths. This can also be seen by the resonant frequencies of transverse modes, which are shifted from the fundamental resonances by integer multiples of $\cos^{-1}(1-L/R)$, where L is the cavity length and R is the radius of curvature. In the limit of infinite R, these frequency shifts are zero, so mode matching is not required. High-finesse Fabry-Perot etalons effectively filter wavefront imperfections by rejecting spatial frequency components outside a narrow angular acceptance [30]. In practice, this means that fine-scale aberrations in the input laser beam are suppressed by the etalon, but, in exchange, the system requires precise control of mirror parallelism and alignment. This topic is discussed in detail in Appendix B. The Rayleigh length of a laser beam is the distance over which the transverse radius increases by a factor of $\sqrt{2}$ and is proportional to the square of the minimum spot size divided by the wavelength. For example, a laser beam at a wavelength of 1 μm with a spot size of 6 cm has a Rayleigh length of about 3 km. If the mirror reflectivity is 99.9%, and the cavity length is 10 cm, then 1000 round-trips is only 100 m, and the beam does not expand significantly. A laser of a 10 W power would produce an intracavity power of 10 kW. For comparison, the Laser Interferometer Gravitational-Wave Observatory (LIGO) routinely has a circulating power of that magnitude or higher in its resonators [31]. To minimize absorption losses and heating of the coatings, near-infrared wavelengths longer than 800 nm are optimum.

To test the above hypothesis, we performed numerical simulations, and the results are shown in Fig. 2. The method and details of the numerical simulation are included in Appendices A and B. The figures show the cavity transmission as the wavelength is scanned; alternatively, the length of the cavity can be changed, and resonances occur for a half-wavelength change. We assume that mirror transmission is $T = 1 - R$, which is justified when scatter and absorption losses are much smaller than transmission. A cavity transmission of unity is expected for a plane wave, and the intracavity circulating power is boosted by a factor of $1/T$. For mirrors with 99% reflectivity, transmission is not affected by the spot size unless it is less than 5 mm. In the case of mirrors with 99.9% reflectivity, the spot size must be larger than 20 mm. These numerical results agree with the heuristic arguments above.

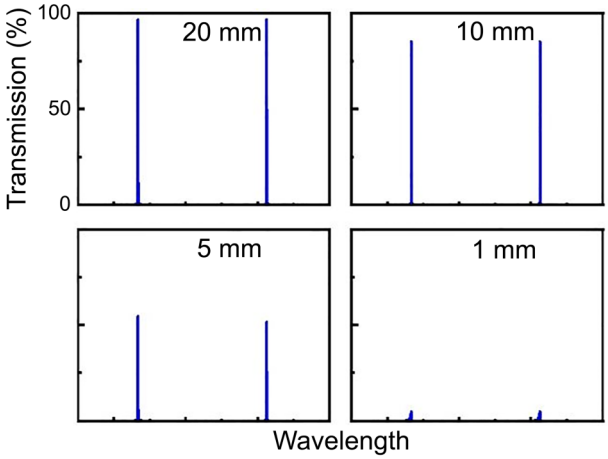

FIG. 2. Numerical simulation of transmission coefficient of a cavity of length 5 cm and mirror reflectivity 99.9%. The spot size is changed from 20 mm to 1 mm.

In addition to isotope separation, the above method can be used for ultrasensitive detection of atomic isotopes. Isotope sensing is especially important for detection of rare isotopes as tracers for metabolism [32] and isotope ratios are sensitive indicators of disease [33]. Small blood or urine samples containing atomic isotopes are already analyzed using mass spectrometers, which have become extremely precise over the years. However, their cost is often prohibitive, and slow sample preparation to isolate the element of interest limits their throughput to a small number of tests per day. Laser spectroscopy can be much more sensitive than mass spectroscopy and has been demonstrated to reach laser shot-noise limited sensitivity using frequency modulation spectroscopy [34]. It is even possible to detect atoms below the standard quantum limit using squeezed light [35]. Detection of atomic isotopes using MRLIS would enable atom counting by detecting the produced ions and removing background signals by modulation of the lasers and lock-in detection of the ion current. This should allow the detection of atomic isotopes limited only by quantum projection noise, which is the ultimate

limit [36]. This would be realized in an atomic beam and does not require a closed cycling transition which is needed for detection of trapped ions or with the atom trap trace analysis method [37–39].

III. APPLICATION OF MRLIS

In this section we discuss an application of MRLIS, presenting a numerical simulation of an ionization scheme for isotope separation. We analyze here the case of Sr, which has a rare isotope, Sr-84, that can be used as a tracer for bone absorption to detect the onset of osteoporosis [40]. This same isotope can also be used to produce the radioisotope Sr-85 which has been proposed for a new test of quantum mechanics [41,42].

A rate-equation model is presented and used to make estimates of ionization fraction in the pulsed and CW cases as a function of ionizing laser power, beam diameter, repetition rate (in the pulsed case), and oven temperature. Saturated optical pumping on the transition to the intermediate state is assumed. The magnitude of expected ac Stark shifts of the transition is also discussed. We estimate that the combination of high intracavity power and long transit time leads to near unity in ionization probability.

A schematic of the relevant energy levels in atomic Sr is shown in Fig. 3. The ionization limit of Sr is 5.695 eV. The ground $^1S_0$ state would first be excited by a laser near 460.9 nm to the $^1P_1$ state which has a decay rate of 2.01×10^8 s^{-1}. A second laser near 405.2 nm would then excite atoms from the $^1P_1$ state to the $^1D_2$ autoionizing state. The quoted spectroscopic data are available online [43].

The ionization cross section is from Ref. [44]. The value reported there is the isotropic cross section $\sigma_{\rm iso}$, appropriate for excitation with unpolarized light. For linearly polarized light the cross section depends on the angle θ between the pump and ionizing laser polarization axes. Assuming that ionization is due to a $J = 1 \rightarrow J = 2$ transition, the dependence is given by Ref. [45]:

$$\sigma_{2i} = \frac{3}{10}\left(3 + \cos^2\theta\right)\sigma_{\rm iso}, \tag{1}$$

or $\sigma_{2i} = 1.2\sigma_{\rm iso}$ for parallel polarizations.

A. Continuous-wave excitation

The laser will be scanned just above the ionization limit to optimize ionization with an autoionizing state, but it may be simpler to find a convenient high-power laser that is above the ionization threshold. Positive ions will be accelerated by an electric field that will remove the desired isotopes from the beam and collect them on a cathode plate.

The optical pumping scheme for ionization of Sr is diagrammed in Fig. 3. Atoms are excited from the ground state $5s^2\,{}^1S_0$ using 460.9-nm light to the intermediate state $5s5p\,{}^1P_1$, and then to the autoionizing state $5p^2\,{}^1D_2$ using 405.2-nm light. Experimental parameters for the numerical results are given in Table I.

Theoretical models of photoionization for isotope separation are described in Refs. [10,46–49]. Here we employ a rate-equation model, valid for CW excitation or when laser pulses are much longer than the excited state lifetime. We assume that the atomic density is low enough that the medium can be considered optically thin. For a uniform atomic beam of density n, interaction cross section $\sigma(\nu)$, and laser interaction path length L, the atomic beam can be considered optically thin if [50]

$$n \ll \frac{1}{L\sigma(\nu)}. \tag{2}$$

For the 405.2-nm transition of Sr, values from Table I suggest that atomic beam densities $n \ll 10^{13}$ cm^{-3} are optically thin. Typical densities for collimated atomic beams from thermal oven sources are in the range 10^7–10^{10} cm^{-3}, satisfying the criterion for optical thinness.

Consider an atomic beam with density n_0 subject to two overlapping laser fields with intensities I_{12} and I_{2i}, respectively, driving transitions from the ground state 1 to an excited state 2 and then ionizing via an autoionizing state i. The level population densities n_1 and n_2 of atoms subject to laser light can be described by the rate equations

$$\begin{aligned}\frac{dn_1}{dt} &= -B_{12}n_1 + (A_{21} + B_{21})\,n_2,\\ \frac{dn_2}{dt} &= B_{12}n_1 - (A_{21} + B_{21} + B_{2i})\,n_2,\end{aligned} \tag{3}$$

where A_{21} is the rate of spontaneous decay from state 2 to 1, $B_{mm'}$ are the stimulated transition rates from $m \rightarrow m'$, and γ is the atomic transit rate through the laser beam.

In general, the populations n_m and transition rates $B_{mm'}$ are each functions of longitudinal atomic velocity v. However, the autoionizing transition is broad, with a full width at half maximum of approximately 1.8 THz, and so B_{2i} can be considered effectively velocity independent [51]. The pump transition is much narrower (about 30 MHz), but if this is narrower than the transverse Doppler distribution, the pump laser can be spectrally broadened, or high enough intensity used to address the entire Doppler distribution. Thus, Eq. (3) can be taken to describe the entire transverse velocity distribution, with all quantities considered velocity independent.

We first consider the case of CW excitation. Each atom with longitudinal velocity v that enters the light beam effectively sees a laser pulse of length equal to the transit time $\tau_t = d/v$, where d is the width of the laser beam. Here, for simplicity, we are neglecting the dependence on transverse velocity and on the shape of the laser beam profile.

Consider a group of atoms with longitudinal velocity v that all enter the beam at the same time. If we assume

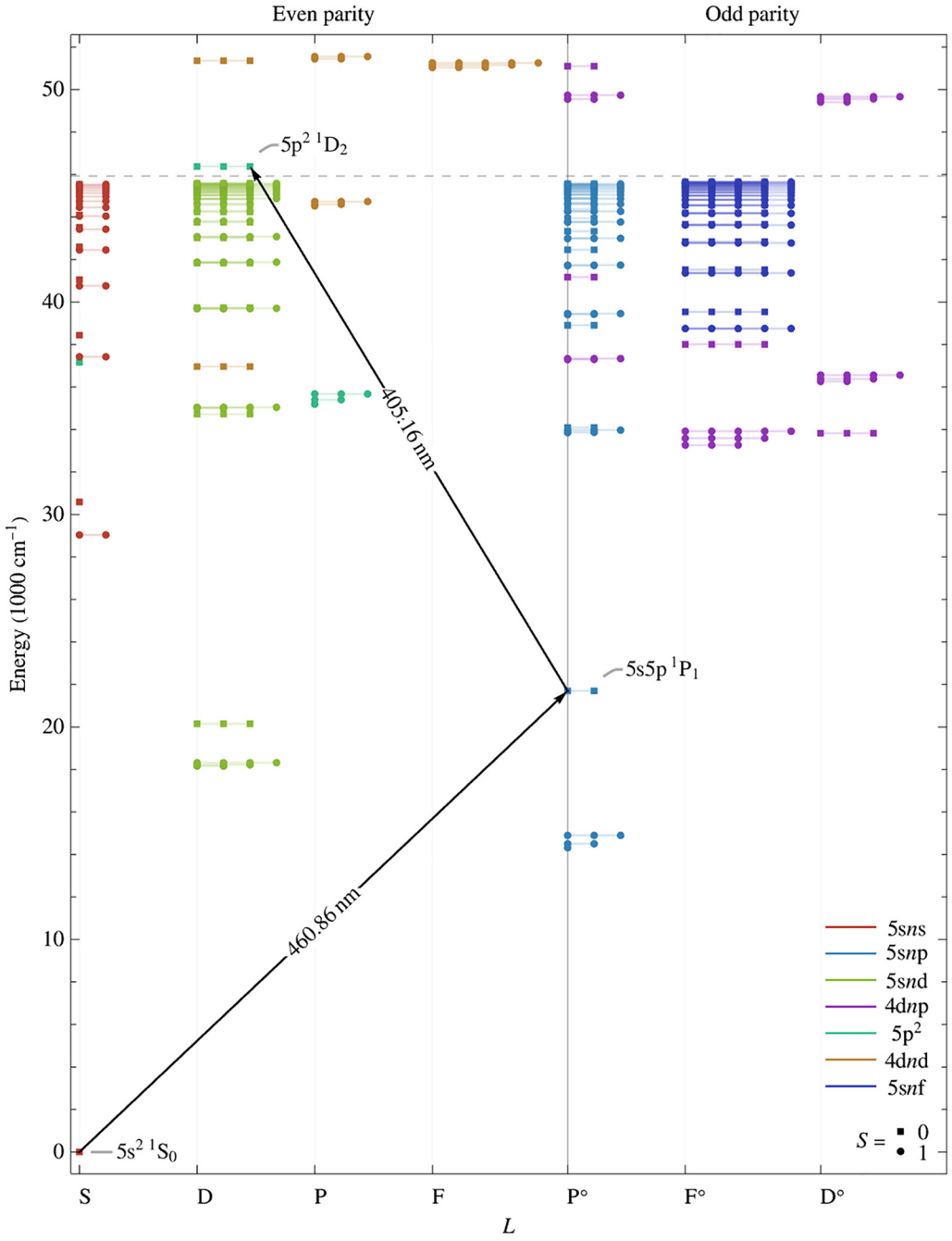

FIG. 3. Optical pumping scheme for photoionization via intermediate state $5s5p\ ^1P_1$ and autoionizing state $5p^2\ ^1D_2$. The total electronic angular momentum of a state (J) can be read out from the diagram as the number of symbols minus one. For example, the $^1P_1$ state is indicated with two squares. Squares indicate $S = 0$ (i.e., a singlet state).

saturation conditions for the $1 \rightarrow 2$ transition (i.e., $B_{12} = B_{21} \gg A_{21}, B_{2i}$), then over short time scales we have a quasi-steady-state condition in which we can set $dn_1/dt = dn_2/dt = 0$ and neglect A_{21} and B_{2i}, so that Eq. (3) reduces to $n_2 = n_1$. In other words, light field 1 continuously equilibrates the level populations so that, at any given time, half of the atoms are in state 1 and half are in state 2.

Over longer time scales (but still shorter than the transit time), the total number of atoms decreases as atoms are ionized. Adding together the two parts of Eq. (3), we find an expression for the rate of increase of ion density n_i, equal to the decrease of the atomic population $n = n_1 + n_2$,

$$\frac{dn_i}{dt} = -\frac{dn}{dt} = B_{2i} n_2 = \frac{B_{2i} n}{2}, \tag{4}$$

TABLE I. Parameters used for the numerical estimates.

Ionization cross section	σ_{2i}	1.2×5450 Mb
Ionization photon energy	$\hbar\omega_{2i}$	4.9×10^{-19} J
Atomic mass	m_a	88 amu
Pulse repetition rate	f_{rep}	1 to 10 kHz
Oven temperature	T	690 to 930 K
Most probable atomic speed in oven	v_0	360 to 420 m/s
Mean longitudinal atomic beam velocity	$\bar{v}$	480 to 560 m/s
Laser beam diameter	d	1 to 5 cm
Circulating ionizing laser power (CW)	P_{2i}	$\leq$5 W $\times$ 100 (buildup)
Average ionizing laser power (pulsed)	$\bar{P}_{2i}$	$\leq$25 W

or, since $n + n_i = n_0$,

$$\frac{dn_i}{dt} = \frac{B_{2i}\,(n_0 - n_i)}{2}. \tag{5}$$

Integrating Eq. (5) over the transit time, we can find the ionization fraction n_i/n_0 for these atoms. For numerical evaluation and plotting it is more convenient to work with the quantity $\eta = 1 - n_i/n_0$, the fraction of atoms that are not ionized. We find

$$\eta_{\text{CW}} = \exp\left(-\int_0^{\tau_t} \frac{1}{2} B_{2i} dt\right). \tag{6}$$

The ionization transition rate is given in terms of the photoionization cross section σ_{2i} by $B_{2i} = \sigma_{2i}\Phi_{2i}$, where $\Phi_{2i} = I_{2i}/(\hbar\omega_{2i})$ is the flux of ionizing photons. Thus the integral in Eq. (6) is given by

$$\int_0^{\tau_t} \frac{1}{2} B_{2i} dt = \frac{\sigma_{2i} I_{2i} \tau_t}{2\hbar\omega_{2i}} = \frac{\sigma_{2i} P_{2i}}{2\hbar\omega_{2i} v d}, \tag{7}$$

where we have used the definition of τ_t and written the light intensity in terms of the light power $P_{2i} = I_{2i} d^2$. Defining the saturation parameter

$$\kappa_{\text{CW}} = \frac{\sigma_{2i} P_{2i}}{2\hbar\omega_{2i} v_0 d}, \tag{8}$$

where v_0 is the most probable atomic speed in the oven from the Maxwell-Boltzmann distribution, we have for the un-ionized fraction of atoms with velocity v,

$$\eta_{\text{CW}}(v) = \exp\left(-\kappa_{\text{CW}} v_0 / v\right). \tag{9}$$

Now the longitudinal velocity distribution $f(v)$ in a thermal atomic beam produced by an oven at temperature T is given by [52]

$$f(v)dv = 2\frac{v^3}{v_0^4} e^{-v^2/v_0^2} dv. \tag{10}$$

It is convenient to write the velocity distribution in terms of a dimensionless velocity $\xi = v/v_0$,

$$f(\xi)d\xi = 2\xi^3 e^{-\xi^2} d\xi. \tag{11}$$

To find the total un-ionized fraction, we multiply Eq. (9) by the velocity distribution $f(\xi)$, and integrate over velocity. This gives

$$\begin{aligned}\eta_{\text{CW}} &= \int_0^\infty f(\xi)\eta_{\text{CW}}(\xi)d\xi = \int_0^\infty 2\xi^3 e^{-\xi^2} e^{-\kappa_{\text{CW}}/\xi} d\xi \\ &= \frac{\kappa_{\text{CW}}^4}{16\sqrt{\pi}} G_{0,3}^{3,0}\left(-2, -\frac{3}{2}, 0 \,\middle|\, \frac{\kappa_{\text{CW}}^2}{4}\right),\end{aligned} \tag{12}$$

where G is the Meijer G-function. We are interested in the regime $\kappa_{\text{CW}} > 1$. Expanding this function in a power series, we find within 1% accuracy in this range that

$$\eta_{\text{CW}} \approx e^{-3(\kappa_{\text{CW}}/2)^{2/3}}\left(0.383\kappa_{\text{CW}}^{-1/3} + 1.579\kappa_{\text{CW}}^{1/3} + 1.023\kappa_{\text{CW}}\right). \tag{13}$$

Substituting numerical parameters from Table I into the expression for κ_{CW}, we find

$$\kappa_{\text{CW}} \approx 4.85 \frac{P_{2i}[\text{W}]}{d[\text{cm}]\sqrt{T[\text{K}]}}, \tag{14}$$

with an upper range of $\kappa_{\text{CW}} \leq 90$. The un-ionized fraction η_{CW} is plotted for a range of κ_{CW} in Fig. 4(a). For a cavity with a 200$\times$ enhancement factor, an input power of at least 1.1 W would achieve ionization efficiency greater than 99%.

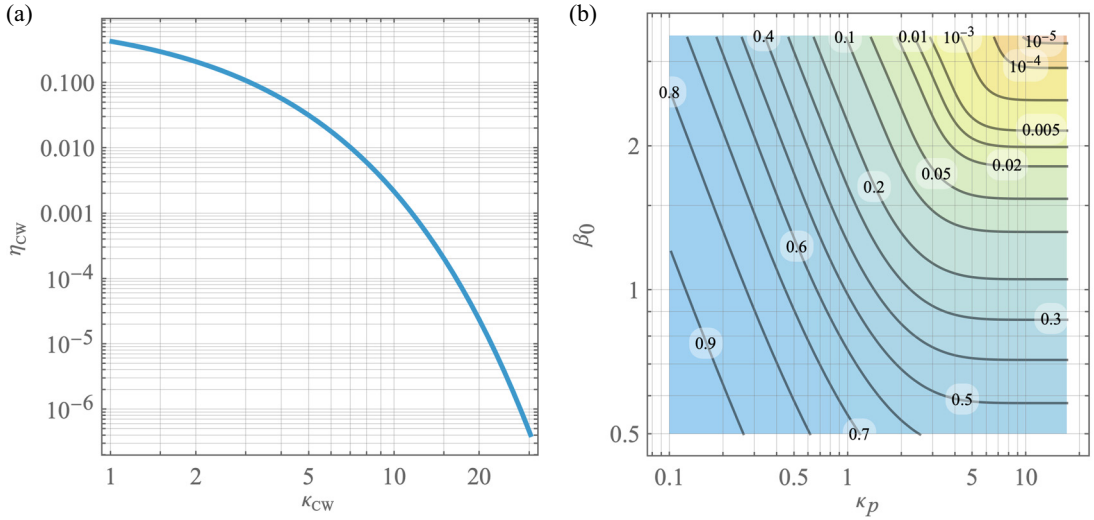

FIG. 4. (a) CW un-ionized fraction η_{CW} and (b) pulsed un-ionized fraction η_p as a function of dimensionless parameters κ_{CW}, κ_p, and β_0. The "useful" ranges of the saturation parameters κ_{CW} and κ_p are plotted, above which further improvement in ionization fraction is negligible.

B. Pulsed excitation

Now consider the case of pulsed excitation, with laser pulses of length τ_p at a repetition rate f_{rep}. We assume that the pulse length is much shorter than the characteristic atomic transit time (i.e., $\tau_p \ll d/v_0$), but still much longer than the equilibration time for optical pumping on the $1 \rightarrow 2$ transition. Then the development proceeds as for the CW case, except that each atom sees an integer number of pulses, the number depending on its velocity and the time that it enters the interaction region.

The number of light pulses that a given atom may be subject to is determined by the ratio of its transit time τ_t through the light beam to the pulse repetition period $1/f_{\mathrm{rep}}$, that is, the quantity $\beta = \tau_t f_{\mathrm{rep}} = f_{\mathrm{rep}} d/v$. Writing $\beta = m + r$, where m is the integer part of β and r is the remainder, a given atom with transit parameter β will be subject to either m or $m+1$ pulses, depending on the time that the atom enters the interaction region; that is, for $0 < \beta < 1$, an atom will see either 0 or 1 pulses, for $1 < \beta < 2$, either 1 or 2 pulses, and so on. The fraction of atoms that see the higher number of pulses is r.

Thus, the un-ionized fraction for atoms with velocity v is

$$\eta_p(v) = (1-r)e^{-m\kappa_p} + re^{-(m+1)\kappa_p}, \tag{15}$$

where m and r both depend on v, and we have obtained the saturation parameter κ_p for the pulsed case,

$$\kappa_p = \frac{\sigma_{2i} P_{2i} \tau_p}{2\hbar\omega_{2i} d^2} = \frac{\sigma_{2i} \bar{P}_{2i}}{2\hbar\omega_{2i} f_{\mathrm{rep}} d^2}, \tag{16}$$

from κ_{CW} by replacing the characteristic transit time with the laser pulse time and writing the peak laser power P_{2i} in terms of the average light power

$$\bar{P}_{2i} = P_{2i} \tau_p f_{\mathrm{rep}}. \tag{17}$$

Multiplying by the atomic velocity distribution and changing variables from v to β gives the integral for the total un-ionized fraction,

$$\eta_p = \int_0^\infty 2\frac{\beta_0^4}{\beta^5} e^{-\beta_0^2/\beta^2} \left[(1-r)e^{-m\kappa_p} + re^{-(m+1)\kappa_p}\right] d\beta, \tag{18}$$

where $\beta_0 = f_{\mathrm{rep}} d/v_0$ is the characteristic transit-time parameter for the velocity distribution.

Using the substitution $\beta = m + r$, we can break up this integral into a sum of integrals over r for each value of m, each integral running from $r = 0$ to 1:

$$\eta_p = \sum_{m=0}^{\infty} \int_0^1 \frac{\beta_0^4}{(m+r)^5} e^{-\beta_0^2/(m+r)^2} \times \left[(1-r)e^{-m\kappa_p} + re^{-(m+1)\kappa_p}\right] dr. \tag{19}$$

Evaluating the integrals, we find that the series can be written as

$$\eta_p = e^{-{\beta_0}^2} - \frac{1}{2}\sqrt{\pi}\beta_0\,(1-\operatorname{erf}\beta_0) + e^{-\kappa_p}\left[\frac{\sqrt{\pi}}{2}\beta_0\left(1-2\operatorname{erf}\beta_0+\operatorname{erf}\left(\frac{\beta_0}{2}\right)\right) + 2e^{-\frac{{\beta_0}^2}{4}} - 2e^{-{\beta_0}^2}\right] + \sum_{m=2}^{\infty} e^{-m\kappa_p}\left[\frac{\sqrt{\pi}}{2}\beta_0\left(\operatorname{erf}\left(\frac{\beta_0}{m-1}\right)-2\operatorname{erf}\left(\frac{\beta_0}{m}\right) + \operatorname{erf}\left(\frac{\beta_0}{m+1}\right)\right) + (m-1)e^{-\frac{{\beta_0}^2}{(m-1)^2}} - 2me^{-\frac{{\beta_0}^2}{m^2}} + (m+1)e^{-\frac{{\beta_0}^2}{(m+1)^2}}\right], \tag{20}$$

where erf is the error function. The terms on the first and second lines describe atoms that are subject to 0 and 1 laser pulses, respectively, while each term of the sum from $m = 2$ to ∞ describes atoms that are subject to m laser pulses. For accurate numerical evaluation, the series can be truncated after a small number of terms. For large enough κ_p, all terms except those on the first line are negligible; in this regime η_p is independent of κ_p.

Substituting numerical parameters into the expressions for κ_p and β_0, we find

$$\kappa_p \approx 6.67\frac{\bar{P}_{2i}[\mathrm{W}]}{d^2\,[\mathrm{cm}^2]\,f_{\mathrm{rep}}[\mathrm{kHz}]} \tag{21}$$

and

$$\beta_0 \approx 0.727\frac{d[\mathrm{cm}]f_{\mathrm{rep}}[\mathrm{kHz}]}{\sqrt{T[\mathrm{K}]}}, \tag{22}$$

with typical values $\kappa_p \leq 45$ and $\beta_0 \leq 2$. The un-ionized fraction η_p is plotted for a range of κ_p and β_0 in Fig. 4(b).

Pulsed lasers operating in the neighborhood of 405 nm capable of matching the ionization efficiency of a cavity-enhanced CW system do not appear to be widely available. For example, a 15-mW pulsed laser with a 10-MHz repetition rate, available from Thorlabs [53], provides an ionization efficiency of 0.04%. Quantel and Ekspla offer optical parametric oscillator-based systems at this wavelength with average power approaching 1 W, but repetition rates in the 10–100 Hz range and consequently very low ionization rates, below 1% [54,55].

C. ac Stark shift

The ac Stark shift of a state due to light interacting with a given transition is of the order of Ω^2/Δ, where Δ is the light detuning from resonance, $\Omega = dE/\hbar$ is the Rabi frequency, d is the dipole matrix element and E is the light electric field amplitude. Writing d in terms of the natural width Γ and wavelength λ of the transition and E in terms of the light intensity I [56] and neglecting numerical factors of order unity, we have

$$\Omega = \frac{1}{\pi}\sqrt{\frac{\Gamma I\lambda^3}{\hbar c}}, \tag{23}$$

resulting in a Stark shift

$$\frac{\Gamma I\lambda^3}{\pi^2\Delta\hbar c}. \tag{24}$$

A significant contribution to the ac Stark shifts of the ground and excited state of the 460.9-nm transition due to the 405.2-nm light is likely to come from the 405.2-nm light interacting with the 460.9-nm transition itself. Using $\lambda = 460.9$ nm, $I = (100\ \mathrm{W})/(3\ \mathrm{cm})^2$, $\Gamma = 1/(5.2\ \mathrm{ns})$, and $\Delta = 2\pi c/(405.2\ \mathrm{nm}) - 2\pi c/(460.9\ \mathrm{nm}) = 5.6\times10^{14}/\mathrm{s}$, we can estimate a Stark shift of the order of 10 kHz. Thus we can conclude that for this case the ac Stark shifts are negligible.

IV. DISCUSSION

Our proposed method for efficient isotope separation based on laser ionization can be compared with the prior method of laser ionization by simple scaling. In that case, pulsed lasers were utilized, with a typical pulse duration of 100 ns and a pulse repetition rate of 10 kHz [6]. The average laser power was in the range of 20 W, as typical with pulsed dye lasers. The enhancement of the ionizing laser in MRLIS with a 1000 finesse cavity, and use of CW solid state lasers with a power of 5–10 W, would provide a comparable average laser intensity to that of the pulsed laser, assuming similar focusing. The interaction time would be about 1000 times longer in the case of MRLIS, addressing all the desired isotopes in the atomic beam, and bringing the ionization probability to near unity. In addition, the use of narrow-band CW lasers would enable high isotopic purity, unlike the previous method where the excitation lasers had large linewidths of the order of 100 MHz, limiting isotopic purity.

The most exciting application of MRLIS is towards production of radioisotopes as an alternative to radiochemistry, due to the small footprint of the system's vacuum chamber, which could fit into standard hot cells. The most compelling case is production of the radioisotope Lu-177 from stable Lu-176 due to the much larger (roughly 700 times) neutron cross section of Lu-176 compared with Yb-176 [57]. The latter stable isotope is currently used to produce Lu-177 which is separated using radiochemistry [24].

In conclusion, the presently proposed isotope-separation technique (MRLIS) is expected to enable new and significantly facilitate existing applications of isotopes in medicine.

ACKNOWLEDGMENTS

We thank Ajith V. Jothikumari for help with figures and for comments on the manuscript. We also thank Logan Hillberry and Henry Chance for comments on the manuscript and acknowledge support from the Sid W. Richardson Foundation and the Novo Nordisk Foundation. M. Raizen is Chairman of the Board of the Pointsman Foundation, which aims to support the production and use of stable isotopes and radioisotopes for medical treatments, diagnostics, and research. M. Raizen holds ownership interest in Atom Mines, LLC, a subsidiary of the Pointsman Foundation. The technologies presented in this publication are related to the interests of both the Pointsman Foundation and Atom Mines, LLC.

DATA AVAILABILITY

The data that support the findings of this article are not publicly available upon publication because it is not technically feasible and/or the cost of preparing, depositing, and hosting the data would be prohibitive within the terms of this research project. The data are available from the authors upon reasonable request.

APPENDIX A: GAUSSIAN BEAM PROPAGATION IN A FABRY-PEROT ETALON

Cavity transmission for a Gaussian beam propagating in a Fabry-Perot etalon was numerically modeled using open-source MATLAB code [29]. The cavity mirror spacing was set at 50 mm, with incident beam spot sizes modeled in a range from 20 mm to 1 mm. Results were computed for both 99% and 99.9% etalon mirror reflectivity. Results for the propagation of incident plane waves in the etalon were also calculated.

For a given etalon, transmission as a function of wavelength is characterized by its interferometer transfer function (ITF),

$$\mathrm{ITF}(\lambda) = \frac{I_{\mathrm{out}}(\lambda)}{I_{\mathrm{in}}(\lambda)}, \tag{A1}$$

where I_{in} is the intensity of light incident on the etalon, and I_{out} is the intensity of light exiting the etalon. The outgoing intensity can be found by the spatial integration of the outgoing field,

$$I_{\mathrm{out}} = \int_0^\infty |U_{\mathrm{out}}(r,z)|^2\, 2\pi r dr, \tag{A2}$$

where r is the radial axis and z is the optical axis, in the direction of the incoming beam. The total outgoing field is the sum of contributions by exiting beams that have made m round trips between the cavity mirrors, where $m = 0, 1, 2, \ldots$. For incident plane waves, these partial beams are expressible as a geometric series, and their sum by an Airy function.

Incident Gaussian beams require a more general approach. Here, we use the method of ray transfer matrix analysis, which allows the performance of ray tracing calculations in cases where the paraxial approximation is valid. In this method, a 2×2 ray transfer matrix (sometimes called an ABCD matrix) operates on a vector representing an incoming light ray, yielding a new vector representing the outgoing ray,

$$\begin{bmatrix} q_{\mathrm{out}} \\ 1 \end{bmatrix} = k \begin{bmatrix} A & B \\ C & D \end{bmatrix} \begin{bmatrix} q_{\mathrm{in}} \\ 1 \end{bmatrix}. \tag{A3}$$

Here, k is a normalization constant, and q is the complex beam parameter defined by

$$\frac{1}{q} = \frac{1}{R} - i\frac{\lambda}{\pi n w^2}, \tag{A4}$$

where R is the Gaussian beam radius of curvature, w is its Gaussian waist size, n is the index of refraction of the material through which the beam is passing, and λ is its wavelength. Because ABCD matrices are linear operators, matrices representing each optical element in a system can be multiplied together to give a single resultant matrix representing the system as a whole:

$$M = M_N M_{N-1} \cdots M_2 M_1. \tag{A5}$$

Modeling a vacuum spaced etalon requires three different kinds of ABCD matrix. The first is M_{refr}, representing the refraction of a ray either entering or exiting the etalon,

$$M_{\mathrm{refr}} = \begin{bmatrix} 1 & 0 \\ 0 & n_1/n_2 \end{bmatrix}, \tag{A6}$$

where n_1 is the index of refraction in the initial medium and n_2 is the index of refraction in the final medium. The second ray-transfer matrix is M_{prop}, which represents the propagation of rays through a homogeneous medium,

$$M_{\mathrm{prop}} = \begin{bmatrix} 1 & h/n \\ 0 & 1 \end{bmatrix}, \tag{A7}$$

where h is the distance propagated (in our case, the mirror-to-mirror distance), and n is the index of refraction of the medium propagated through (vacuum, so here $n = 1$). The third and last matrix is M_{refl}, which gives the reflection of

rays from a planar surface,

$$M_{\text{refl}} = \begin{bmatrix} 1 & 0 \\ 0 & 1 \end{bmatrix}. \tag{A8}$$

Conceptually, it is natural to model the propagation of the beam through the etalon in three parts: M_{in}, in which a ray enters the etalon through the first mirror; M_{cav}, in which the ray bounces back and forth between the cavity mirrors; and M_{out}, in which the ray exits the etalon. M_{in} only involves refraction by the first mirror,

$$M_{\text{in}} = M_{\text{refr}}. \tag{A9}$$

For M_{cav}, consider the constituent matrices of a round trip through the interior of the etalon: (1) propagation through the interior to the surface of the second mirror; (2) reflection from the second mirror's surface; (3) propagation back to the first mirror; and (4) reflection from the first mirror's surface. In matrix form,

$$M_{\text{cav}} = M_{\text{refl}}^{\leftarrow} M_{\text{prop}}^{\leftarrow} M_{\text{refl}} M_{\text{prop}}. \tag{A10}$$

The matrix M_{out}, representing the ray transmitted through the cavity, is comparatively straightforward: propagation to the second mirror surface, followed by refraction through the second mirror to exit the etalon,

$$M_{\text{out}} = M_{\text{refr}} M_{\text{prop}}. \tag{A11}$$

Now M_{in} and M_{out} occur exactly once for each transmitted ray, but the number m of round trips within the cavity can be any non-negative integer, so the overall system matrix for any possible transmitted ray has the form

$$M = M_{\text{out}} \left(M_{\text{cav}}\right)^m M_{\text{in}}. \tag{A12}$$

From this system matrix, the transmitted field can be computed from the relation

$$U_{\text{out}}(r, z; M) = \frac{1}{A + B/q\left(z_{\text{in}}\right)} \exp\left(-ik \frac{r^2}{2q\left(z_{\text{out}}\right)}\right), \tag{A13}$$

where z_{in} and z_{out} are the axial positions at the entrance and exit of the etalon, respectively.

The ABCD ray-tracing model does not capture changes in field amplitude, so that must be included in the final summation of contributions to the field from all transmitted beams,

$$U_{\text{out}}(r, z) = \sum_{m=0}^{\infty} A_m U_m, \quad A_m = t_1 t_2 \left(r_1 r_2\right)^m. \tag{A14}$$

Here, t_1, t_2, and r_1, r_2 are the transmittivity and reflectivity coefficients of the first and second mirrors. The above provides a method to compute the ITF for any chosen wavelength, given the incoming beam spot and waist size, the indices of refraction for intra- and extracavity material, the mirror-to-mirror spacing, and the reflectivity of each mirror.

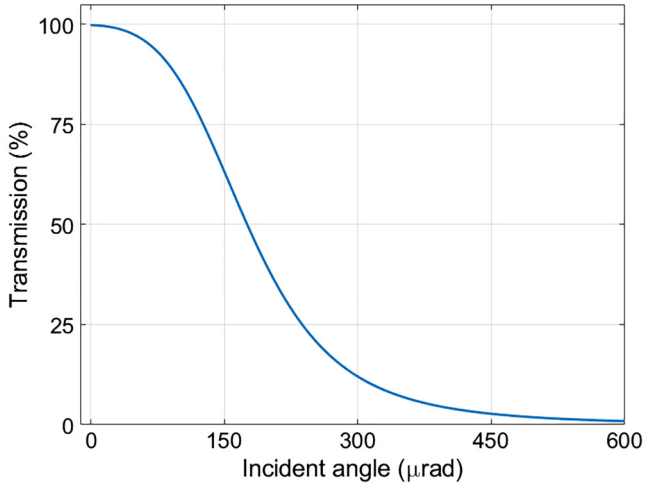

FIG. 5. Numerical simulation of the effect of laser beam incidence angle on cavity transmission. Cavity is 5 cm in length, mirror reflectivity is 99%, and laser spot size is 10 mm.

While the number of cavity round trips m used in computing the transmitted field ranges from zero to infinity, because the partial field contribution becomes smaller and smaller for higher-m terms, the number of computed round trips can be truncated at a finite value. This truncation was chosen by considering the output ITF values to have converged once the most recent term changes the overall transmitted field amplitude by less than 0.001%, typically $m \sim 100$. To capture fine details, 10^3 points/nm were computed in the vicinity of the transmission peaks, with 10^2 points/nm in the interpeak region. The plane-wave computations were performed by setting the spot size to several orders of magnitude larger than the cavity dimensions. An output of this computation for representative values of cavity length, mirror reflectivity, and laser spot size is shown in Fig. 5.

APPENDIX B: INCIDENCE ANGLE AND MIRROR NONPARALLELISM

If the input laser beam is tilted at an angle θ_t relative to the etalon, each successive reflection inside the etalon is slightly displaced. This displacement is called walkoff. The walkoff per round trip is

$$\Delta_{\text{walk}} = 2d \tan\theta_t. \tag{B1}$$

As the beam is displaced by Δ_{walk} relative to the previous pass, the overlap between the two profiles is reduced. The normalized field overlap between $u(r)$ and a displaced

copy $u(r-\Delta)$ is given by

$$\eta_{\text{overlap}}(\Delta) = \frac{\left|\iint u(\mathbf{r})u(\mathbf{r}-\Delta)d^2r\right|}{\sqrt{\iint |u(\mathbf{r})|^2 d^2r \iint |u(\mathbf{r}-\Delta)|^2 d^2r}}, \quad \text{(B2)}$$

where

$$u(\mathbf{r}) = \exp\left(-\frac{r^2}{w_0^2}\right) \quad \text{(B3)}$$

and w_0 is the beam waist. Making the reasonable assumption that both beams have the same width and power, the above simplifies to

$$\eta_{\text{overlap}}(\Delta) = \exp\left(-\frac{\Delta_{\text{walk}}^2}{2w_0^2}\right). \quad \text{(B4)}$$

For the mth round trip, this amplitude field factor becomes

$$a_{\text{mode}}(m) = \exp\left(-\frac{(m\Delta_{\text{walk}})^2}{2w_0^2}\right). \quad \text{(B5)}$$

After a number of round trips, the beam will begin to walk off the mirror entirely. The power fraction of an offset two-dimensional Gaussian that passes through a circular aperture of radius a is given by the formula

$$P_{\text{pass}}(\Delta) = \frac{2\pi}{\pi w_0^2/2}\int_0^a re^{-\frac{2(r^2+\Delta^2)}{w_0^2}} I_0\left(\frac{4r\Delta}{w_0^2}\right)dr, \quad \text{(B6)}$$

where I_0 is a modified Bessel function [58]. The corresponding field amplitude factor is $a_{\text{ap}}(\Delta) = \sqrt{P_{\text{pass}}(\Delta)}$. The transmitted field summed over m round trips is

$$E_{\text{out}}(\lambda,\theta) = t^2\sum_{m=0}^{m_{\max}} a_m\left(r^2e^{i\delta}\right)^m, \quad \text{(B7)}$$

where $t=\sqrt{1-R}$ is the transmission amplitude, $r=\sqrt{R}$ is the reflection amplitude, $a_m = a_{\text{mode}}(m)\cdot a_{\text{ap}}(m)$ is the combined Gaussian overlap and aperture loss factors, and $m_{\max}$ is chosen so that additional round trips no longer significantly contribute to the sum. δ is the single round-trip optical phase shift,

$$\delta = \frac{2\pi}{\lambda}\cdot(2nd\cos\theta_t), \quad \text{(B8)}$$

where n is the refractive index of the intracavity medium and d is the physical distance between the etalon mirrors. The transmission T is given by

$$T(\lambda,\theta) = |E_{\text{out}}|^2. \quad \text{(B9)}$$

If the input laser beam is instead normally incident on the etalon, but one of the mirrors has a small tilt θ relative to the other in an azimuthal direction ϕ, the gap between mirrors is given by

$$d(x,y) = d_0 + \theta(x\cos\phi + y\sin\phi). \quad \text{(B10)}$$

x,y are coordinates in the mirror plane, with the beam center at $(0,0)$. A numerical simulation illustrating how this affects cavity transmission is shown in Fig. 6. The round-trip phase varies across the beam footprint as

$$\delta(x,y;\lambda) = \frac{4\pi nd(x,y)}{\lambda}. \quad \text{(B11)}$$

The resonance condition is $\delta = 2m\pi$, so different parts of the beam see different resonances, leading to inhomogeneous broadening. The Airy transmission is

$$T(\lambda) = \frac{1}{1+F\sin^2\left(\frac{\delta}{2}\right)}, \quad \text{(B12)}$$

where

$$F = \frac{4R}{(1-R)^2}. \quad \text{(B13)}$$

The effective ITF can be modeled as the Gaussian-weighted average of the local transmissions,

$$T_{\text{avg}}(\lambda) = \frac{\iint_{\text{aperture}} I(x,y)T(\lambda;x,y)dxdy}{\iint_{\text{aperture}} I(x,y)dxdy}, \quad \text{(B14)}$$

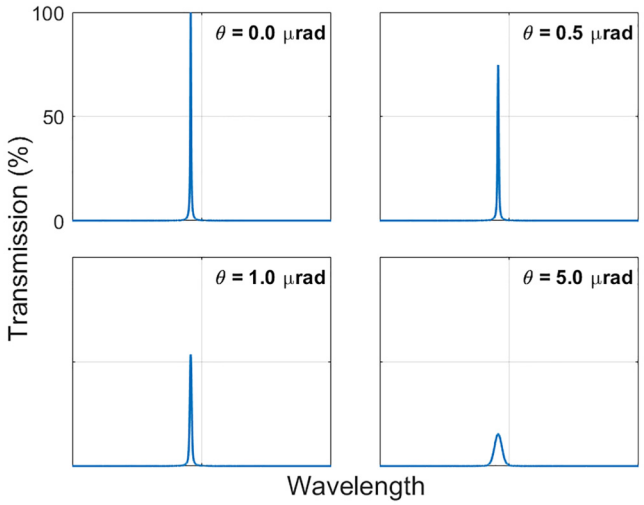

FIG. 6. Numerical simulation of the effect of mirror nonparallelism on cavity transmission. Cavity is 5 cm in length, mirror reflectivity is 99%, and laser spot size is 10 mm. θ is the mirror wedge angle.

where the beam $I(x,y)$ is given by

$$I(x,y) = \exp\left[-\frac{2\left(x^2+y^2\right)}{w^2}\right]. \tag{B15}$$

In this paper, we use a discrete $N_{xy} \times N_{xy}$ grid with normalized weights $W(x,y)$ given by

$$W_{ij} = \frac{I_{ij}}{\sum_{m,n} I_{mn}}, \tag{B16}$$

where $I(x,y) = 0$ for points outside the etalon mirrors.

[1] World Nuclear Association, "Radioisotopes in Medicine," Information Library: Non-Power Nuclear Applications / Radioisotopes & Research (updated 10 January 2025), https://world-nuclear.org/information-library/non-power-nuclear-applications/radioisotopes-research/radioisotopes-in-medicine.

[2] Y. K. Lim and D. Kim, Brachytherapy: A comprehensive review, Prog. Med. Phys. **32**, 25 (2021).

[3] S. J. Goldsmith, Targeted radionuclide therapy: A historical and personal review, Semin. Nucl. Med. **50**, 87 (2020).

[4] G. Crişan, N. S. Moldovean-Cioroianu, D.-G. Timaru, G. Andrieş, C. Căinap, and V. Chiş, Radiopharmaceuticals for PET and SPECT imaging: A literature review over the last decade, Int. J. Mol. Sci. **23**, 5023 (2022).

[5] I.-Y. Kim, S.-H. Suh, I.-K. Lee, and R. R. Wolfe, Applications of stable, nonradioactive isotope tracers in in vivo human metabolic research, Exp. Mol. Med. **48**, e203 (2016).

[6] L. Love, Electromagnetic separation of isotopes at Oak Ridge: An informal account of history, techniques, and accomplishments, Science **182**, 343 (1973).

[7] J. W. Beams and F. Haynes, The separation of isotopes by centrifuging, Phys. Rev. **50**, 491 (1936).

[8] U.S. Department of Energy, Nuclear Science Advisory Committee, Isotopes Subcommittee, Meeting Isotope Needs and Capturing Opportunities for the Future: The 2015 Long Range Plan for the DOE-NP Isotope Program, DOE Technical Report No. OSTI ID:1298983 (U.S. Department of Energy, Washington, D.C., July 2015).

[9] Oak Ridge National Laboratory, "Generations of Separation: EMIS Keeps Improving," Oak Ridge National Laboratory News, May 15, 2023, https://www.ornl.gov/news/generations-separation-emis-keeps-improving.

[10] P. A. Bokhan, V. V. Buchanov, N. V. Fateev, M. M. Kalugin, M. A. Kazaryan, A. M. Prokhorov, and D. E. Zakrevskii, *Laser Isotope Separation in Atomic Vapor* (Wiley-VCH, Weinheim, 2006).

[11] H. Park, D.-H. Kwon, Y. H. Cha, T.-S. Kim, J. Han, K.-H. Ko, D.-Y. Jeong, and C.-J. Kim, Stable isotope production of ^{168}Yb and ^{176}Yb for industrial and medical applications, J. Nucl. Sci. Technol. **45**, 111 (2008).

[12] D.-Y. Jeong, K.-H. Ko, G. Lim, and C.-J. Kim, Method for isotope separation of thallium, US Patent 7,323,651 (2008).

[13] M. Suryanarayana and M. Sankari, Numerical study of the laser isotope separation of optically pumped ^{102}Pd, Sci. Rep. **14**, 4080 (2024).

[14] M. Suryanarayana, Laser isotope separation of ^{203}Tl through pulsed laser optical pumping, J. Opt. Soc. Am. B **41**, 311 (2024).

[15] A. Baranov and E. Tournié, *Semiconductor Lasers: Fundamentals and Applications* (Woodhead Publishing/Elsevier, Cambridge, UK, 2013).

[16] M. Guina, A. Rantamäki, and A. Härkönen, Optically pumped VECSELs: Review of technology and progress, J. Phys. D: Appl. Phys. **50**, 383001 (2017).

[17] M. Jerkins, I. Chavez, U. Even, and M. Raizen, Efficient isotope separation by single-photon atomic sorting, Phys. Rev. A **82**, 033414 (2010).

[18] M. G. Raizen and B. Klappauf, Magnetically activated and guided isotope separation, New J. Phys. **14**, 023059 (2012).

[19] T. R. Mazur, B. Klappauf, and M. G. Raizen, Demonstration of magnetically activated and guided isotope separation, Nat. Phys. **10**, 601 (2014).

[20] M. G. Raizen and B. G. Klappauf, Isotope separation by magnetic activation and separation, US Patent 8,672,138 (2014).

[21] S. Banerjee, M. Pillai, and F. Knapp, Lutetium-177 therapeutic radiopharmaceuticals: Linking chemistry, radiochemistry, and practical applications, Chem. Rev. **115**, 2934 (2015).

[22] H. Metcalf, *Laser Cooling of Atoms* (Springer, Berlin, 1999).

[23] E. Anciaux, G. Stratis, and M. Raizen, Brightening of a supersonic beam of neutral atoms, Phys. Scr. **93**, 124009 (2018).

[24] J.-V. Kratz, *Nuclear and Radiochemistry: Fundamentals and Applications* (John Wiley & Sons, Hoboken, NJ, 2022).

[25] N. V. Vitanov, A. A. Rangelov, B. W. Shore, and K. Bergmann, Stimulated Raman adiabatic passage in physics, chemistry, and beyond, Rev. Mod. Phys. **89**, 015006 (2017).

[26] A. E. Siegman, *Lasers* (University Science Books, Mill Valley, CA, 1986).

[27] I. Riou, N. Mielec, G. Lefèvre, M. Prevedelli, A. Landragin, P. Bouyer, A. Bertoldi, R. Geiger, and B. Canuel, A marginally stable optical resonator for enhanced atom interferometry, J. Phys. B: At. Mol. Opt. Phys. **50**, 155002 (2017).

[28] S. Miyoki, M. Ohashi, K. Waseda, H. Karoji, and T. Tomaru, Manufacture of a 10-km-scale radius-of-curvature surface by use of a thin-film coating technique, Opt. Lett. **30**, 1399 (2005).

[29] D. Martin-Sanchez, J. Li, D. M. Marques, E. Z. Zhang, P. R. Munro, P. C. Beard, and J. A. Guggenheim, ABCD transfer matrix model of Gaussian beam propagation in Fabry-Perot etalons, Opt. Express **30**, 46404 (2022).

[30] N. Ismail, C. C. Kores, D. Geskus, and M. Pollnau, Fabry-Pérot resonator: spectral line shapes, generic and related airy distributions, linewidths, finesses, and performance at low or frequency-dependent reflectivity, Opt. Express **24**, 16366 (2016).

[31] J. R. Smith *et al.* (LIGO Scientific Collaboration), The path to the enhanced and advanced LIGO gravitational-wave detectors, Class. Quantum Gravity **26**, 114013 (2009).

[32] S. A. Abrams, Using stable isotopes to assess mineral absorption and utilization by children, Am. J. Clin. Nutr. **70**, 955 (1999).
[33] K. Schilling, F. Larner, A. Saad, R. Roberts, H. M. Kocher, O. Blyuss, A. N. Halliday, and T. Crnogorac-Jurcevic, Urine metallomics signature as an indicator of pancreatic cancer, Metallomics **12**, 752 (2020).
[34] G. C. Bjorklund, M. Levenson, W. Lenth, and C. Ortiz, Frequency modulation (FM) spectroscopy: Theory of lineshapes and signal-to-noise analysis, Appl. Phys. B **32**, 145 (1983).
[35] E. Polzik, J. Carri, and H. Kimble, Spectroscopy with squeezed light, Phys. Rev. Lett. **68**, 3020 (1992).
[36] W. Itano, J. Bergquist, J. Bollinger, J. Gilligan, D. Heinzen, F. Moore, M. Raizen, and D. Wineland, Erratum: Quantum projection noise: Population fluctuations in two-level systems [Phys. Rev. A 47, 3554 (1993)], Phys. Rev. A **51**, 1717 (1995).
[37] C. Chen, Y. Li, K. Bailey, T. O'Connor, L. Young, and Z. Lu, Ultrasensitive isotope trace analyses with a magneto optical trap, Science **286**, 1139 (1999).
[38] Z.-T. Lu, P. Schlosser, W. Smethie Jr, N. Sturchio, T. Fischer, B. Kennedy, R. Purtschert, J. Severinghaus, D. Solomon, T. Tanhua *et al.*, Tracer applications of noble gas radionuclides in the geosciences, Earth-Sci. Rev. **138**, 196 (2014).
[39] USTC Laser Laboratory for Trace Analysis and Precision Measurements, "A Primer on Atom Trap Trace Analysis (ATTA)," USTC Events (accessed 10 September 2025), https://atta.ustc.edu.cn/en-us/events/attaprimer.html.
[40] A. Anbar, J. Skulan, G. Gordon, and J. Morgan, Isotopic biomarkers for rapid assessment of bone mineral balance in biomedical applications, US Patent 9,261,519 (2016).
[41] M. G. Raizen, D. E. Kaplan, and S. Rajendran, Do atoms age? Phys. Lett. B **832**, 137224 (2022).
[42] M. G. Raizen, New tests of quantum mechanics with unstable nuclei, Phys. Lett. B **865**, 139480 (2025).
[43] National Institute of Standards and Technology, "Atomic Spectra Database: Ground Levels and Ionization Energies for the Neutral Atoms," NIST Physics Reference Data, https://physics.nist.gov/PhysRefData/ASD/lines_form.html.
[44] S. Q. Haq, S. Mahmood, N. Amin, Y. Jamil, R. Ali, and M. Baig, Measurements of photoionization cross sections from the 5s5p $^1P_1$ and 5s6s $^1S_0$ excited states of strontium, J. Phys. B: At. Mol. Opt. Phys. **39**, 1587 (2006).
[45] W. Mende, K. Bartschat, and M. Kock, Near-threshold photoionization from the Sr I (5s5p) $^1P^o_1$ state, J. Phys. B: At. Mol. Opt. Phys. **28**, 2385 (1995).
[46] S. Borisov, M. Kuz'mina, and V. Mishin, A study of isotopically selective photoionization of ytterbium atoms for laser isotope separation, J. Russ. Laser Res. **17**, 332 (1996).
[47] S. Borisov, M. A. Kuz'mina, and V. A. Mishin, Selective photoionisation of ^{168}Yb in an extended optically dense medium, Quantum Electron. **28**, 169 (1998).
[48] A. N. Tkachev and S. I. Yakovlenko, Multistage photoionisation of ytterbium, Quantum Electron. **26**, 839 (1996).
[49] A. N. Tkachev and S. I. Yakovlenko, On laser rare-isotope separation, Quantum Electron. **33**, 581 (2003).
[50] W. Demtröder, *Laser Spectroscopy: Vol. 1: Basic Principles* (Springer, Berlin, 2008), 4th ed.
[51] C. Dai, S. Hu, and J. Lu, Multistep excitation of autoionizing states of neutral strontium, J. Quant. Spectrosc. Radiat. Transfer **56**, 255 (1996).
[52] N. F. Ramsey, *Molecular Beams, Vol. 20 of International Series of Monographs on Physics* (Clarendon Press, Oxford, 1956).
[53] Thorlabs, "NPL Series of Nanosecond Pulsed Laser Systems," Thorlabs Product Information, https://www.thorlabs.com/newgrouppage9.cfm?objectgroup_id=10823&pn=NPL41B#ad-image-0 (accessed 10 September 2025).
[54] Ekspla, "Narrow-Linewidth Tunable Wavelength Laser NT260 – Specifications," Ekspla Product Information, https://ekspla.com/products/narrow-linewidth-tunable-wavelength-laser-nt260/#specifications (accessed 10 September 2025).
[55] Quantel Laser, "Peacock XT-355/405nm 2850 μm," Quantel Product Information, https://www.quantel-laser.com/en/products/item/peacock-xt-355-405-nm-2850-um.html (accessed 10 September 2025).
[56] M. Auzinsh, D. Budker, and S. Rochester, *Optically Polarized Atoms: Understanding Light-Atom Interactions* (Oxford University Press, Oxford, 2010).
[57] A. Dash, M. R. A. Pillai, and F. F. Knapp, Production of ^{177}Lu for targeted radionuclide therapy: available options, Nucl. Med. Mol. Imaging **49**, 85 (2015).
[58] T. S. Khwaja and S. A. Reza, Low-cost Gaussian beam profiling with circular irises and apertures, Appl. Opt. **58**, 1048 (2019).